buildings

MDPI

Article

Soil Conditioning for EPB Shield Tunnelling in Sand-Cobble Strata: An Integrated Laboratory-DEM Approach

Weimiao Zhang *, Zhe Liu, Jiahui Zhang, Tingyuan Wang and Zhiyong Yang

School of Mechanics and Civil Engineering, China University of Mining and Technology (Beijing), Haidian District, Beijing 100083, China; bqt2400603018@student.cumtb.edu.cn (Z.L.); bqt2500602022@student.cumtb.edu.cn (J.Z.); bqt2600602021@student.cumtb.edu.cn (T.W.); yangzy1010@cumtb.edu.cn (Z.Y.)

* Correspondence: zqt2400603075@student.cumtb.edu.cn

Abstract

In large-particle sandy cobble strata, laboratory slump and impermeability tests can evaluate the workability of conditioned soil but do not adequately resolve its mechanical behaviour or the surface-settlement response during shield tunnelling. Thus, this study proposes a method for determining a soil-conditioning scheme by combining laboratory tests with full-scale discrete element simulations. For a Beijing metro shield project, the injection parameters were determined through conditioning-agent performance tests and slump tests. A full-scale discrete element model was established and calibrated using triaxial compression and slump tests. Cutter forces, cutterhead loads and surface settlement were used as indices to determine the preferred conditioning scheme. The results show that a 5% foaming-agent solution and an 8% bentonite slurry exhibited favourable preparation performance. When the bentonite injection ratio (BIR) was 12% and the foam injection ratio (FIR) was 30% or 40%, the conditioned soil exhibited favourable flowability and workability. At a BIR of 12%, increasing the FIR from 30% to 40% reduced the mean cutting force of the ripper cutters, mean total thrust and mean cutterhead torque by 19.10%, 22.29% and 8.09%, while the maximum settlement decreased by 25.3%. Field and simulated settlement trends agreed, with a final relative difference of 15%.

Keywords: sandy cobble strata; soil conditioning; earth pressure balance shield; discrete element modelling; shield tunnelling response

1. Introduction

Earth pressure balance (EPB) shields are widely used for urban tunnelling because they accommodate varied ground conditions, limit construction disturbance, control surface settlement and support high advance rates. In broadly graded, highly permeable sandy cobble strata with a high coarse-particle content, excavated soil has poor flowability and plasticity and often fails to meet EPB operating requirements [1]. Appropriate soil conditioning can improve the flowability and cohesion of sandy cobble soil [2], reducing cutter forces, cutterhead torque and cutter wear while increasing excavation efficiency [3].

Previous work on conditioning-agent selection and dosage for EPB tunnelling falls into three broad areas: formulation optimisation, mechanisms of combined conditioning and ground-specific mix design. Sun et al. [4] optimised a foaming-agent formulation comprising surfactants, foam stabilisers, viscosity modifiers and inorganic salts, and assessed its performance using slump, friction and direct shear tests. Sun and Zhao [5] formulated a

Check for updates

Academic Editor: Eugeniusz Koda

Received: 15 September 2026
Revised: 8 October 2026
Accepted: 10 October 2026
Published: 13 October 2026

Copyright: © 2026 by the authors. Licensee MDPI, Basel, Switzerland. This article is an open access article distributed under the terms and conditions of the Creative Commons Attribution (CC BY) license.

composite slurry from bentonite, xanthan gum, soda ash and clay particles, and determined suitable proportions for sandy cobble strata. For combined systems, Ling et al. [6] conducted high-gradient permeability tests and found that the bentonite injection ratio (BIR) had a greater influence on permeability than the foam injection ratio (FIR). Wang et al. [7] generated foam directly in bentonite slurry and assessed how the resulting foam-slurry system affected the permeability, flowability and volumetric stability of coarse-grained soil under high water pressure. A subsequent study [8] examined the stability of this system in water-rich sand and its effects on flowability, volumetric stability and impermeability. The foam-slurry system met the conditioning requirements while using 3.0–8.2% less slurry than slurry-only conditioning. Nong et al. [9] used a full-factorial design to quantify the main and interactive effects of polymer, foaming-agent and bentonite-slurry concentrations, providing a basis for multicomponent mix design.

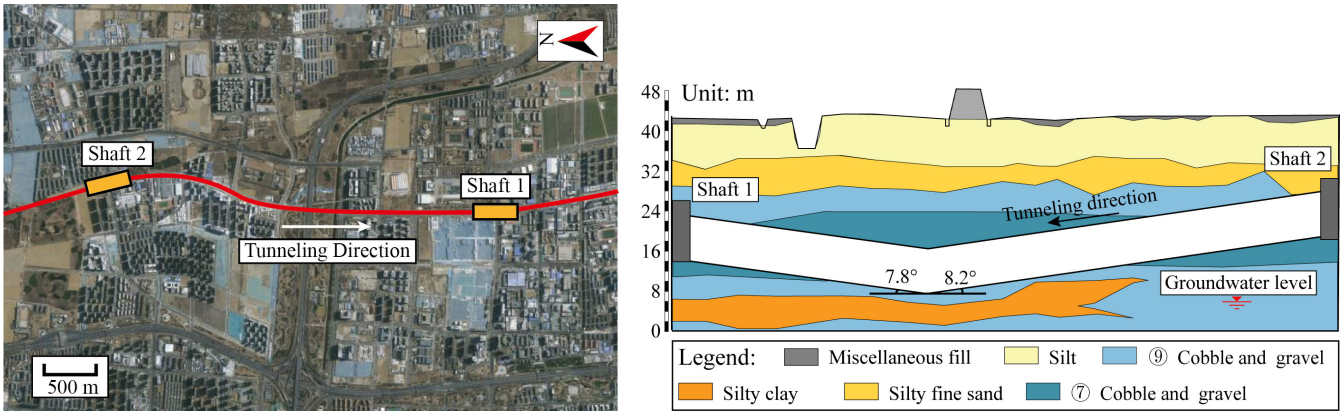
Research has progressed beyond laboratory workability tests to examine cutterhead loads, performance in complex ground and optimisation of field parameters. Lee et al. [10] used scaled excavation tests to evaluate the effects of fine-particle content, water content and foam injection on torque, cutter mass loss and soil slump. Yang et al. [11] combined triaxial, abrasion and sliding tests to characterise the time-dependent mechanical and frictional properties of conditioned sand, and developed a cutterhead-torque model that agreed with field measurements. Laboratory and field tests by Li et al. [12] showed that combined conditioning with foam, polymer and bentonite improved the flowability, plasticity and impermeability of water-rich sandy soil and supported stable excavation. Zhang et al. [13] developed ground-specific conditioning parameters for different sand-to-rock area ratios; scaled tests and field data confirmed their effects on thrust, torque and chamber pressure. Wang et al. [14] compared the shear and pore responses of slurry, foam and foam–slurry systems. In the field, combined foam and slurry conditioning reduced cutterhead torque by approximately 37% without spewing. Wang et al. [15] used tunnelling data to optimise conditioning-agent consumption, reducing total thrust and cutterhead torque by at least 15% and 13%, respectively, while increasing the mean advance rate by more than 38%. In numerical studies, Qu et al. [16] coupled the discrete element and finite difference methods (DEM-FDM) and represented conditioning by varying the interparticle friction coefficient. Cutterhead torque was more sensitive to the degree of conditioning than thrust. Lee et al. [17] subsequently incorporated foam conditioning into a coupled DEM-FDM tunnelling model and found reductions in cutterhead torque, shield thrust and cutter forces.

Existing studies generally determine soil-conditioning schemes from laboratory indices such as slump and impermeability. These tests characterise the flowability, plasticity, impermeability and workability of conditioned soil, but do not directly quantify cutter forces, cutterhead loads or surface settlement. Few studies have systematically linked conditioning parameters to these construction responses, despite their importance during EPB shield tunnelling in sandy cobble strata. Here, we address this gap using the No. 2 southbound shield shaft-No. 1 ventilation shaft project in the Cigezhuang–Caoqiao section of Phase I of the Beijing New Airport Metro Line. Conditioning-agent performance and slump tests first identified injection parameters that met the flowability and workability requirements. We then used full-scale DEM simulations to predict cutter forces, cutterhead loads and surface settlement for the candidate schemes and to select the preferred scheme. This integrated approach links laboratory workability assessment with construction-scale responses when designing soil-conditioning schemes for sandy cobble strata. The main methodological contribution of this study is the use of a full-scale DEM model to extend the evaluation of candidate conditioning schemes from laboratory workability to shield-tunnelling responses.

2. Project Overview

2.1. Project Description

The study section lies between No. 2 southbound shield shaft and No. 1 ventilation shaft in the Cigezhuang–Caoqiao section of Phase I of the Beijing New Airport Metro Line (Figure 1a). Hereafter, it is referred to as the MGZ-CQ-S2-V1 section. Located in north-western Daxing District, Beijing, the shield section extends for 4330 m. From Daxing Airport, the line runs north through Cigezhuang Station before entering the underground section towards Caoqiao Station.



(**a**) (**b**)

Figure 1. Plan view and geological conditions along the MGZ-CQ-S2-V1 section: (**a**) Plan view of the MGZ-CQ-S2-V1 section; (**b**) Longitudinal geological profile of the MGZ-CQ-S2-V1 section.

The MGZ-CQ-S2-V1 section comprises miscellaneous fill, silt, cobble and rounded gravel layers ⑦ and ⑨, silty clay, fine sand and silt (Figure 1b). The tunnel runs mainly through layers ⑦ and ⑨ at depths of 14.3–26.1 m. The left and right sections of the tunnel have gradients of 7.8° and 8.2°, respectively. In layer ⑦, particles larger than 20 mm constitute more than 60% of the mass, the maximum particle size exceeds 150 mm, and fine sand fills the interparticle voids. The corresponding coarse-particle fraction in layer ⑨ is approximately 70%, and the maximum particle size exceeds 200 mm. The groundwater table remained below the tunnel invert throughout the alignment; thus, the entire tunnel excavation zone was above the groundwater table. These particle-size distributions classify the ground as large-particle sandy cobble strata. The abundance of quartz-rich cobbles and gravels makes the strata highly abrasive. The coarse particles also form well-developed voids that favour seepage-channel formation, increasing the risks of face instability during excavation. Together, these conditions complicate soil conditioning and require a project-specific conditioning scheme.

2.2. Cutterhead Layout

The MGZ-CQ-S2-V1 section was excavated using an EPB shield with a diameter of 9114 mm and a cutterhead opening ratio of 55%. The cutterhead comprised six main spokes and six auxiliary spokes and carried a fish-tail cutter, ripper cutters and scrapers (Figure 2). The central fish-tail cutter was 450 mm high. Each ripper cutter was 280 mm wide and 80 mm thick, with a spacing of 85 mm. The ripper cutters were installed at two protrusion heights normal to the cutterhead: 50 cutters at 145 mm and 74 at 175 mm. Scrapers were installed on both sides of the ripper cutters. Each scraper was 100 mm wide and 150 mm thick, with a spacing of 120 mm. In the direction normal to the cutterhead, 108 scrapers were 110 mm high and 50 were 90 mm high. A further 36 peripheral ripper cutters were installed around the cutterhead edge, comprising 12 cutters at 145 mm and 24 at 175 mm.

Nine conditioning-agent injection cutters were installed to condition the ground ahead of the cutterhead: three in the central region (≤4650 mm), four in the face region (4650–7200 mm) and two in the peripheral region (7200–9114 mm). Each could deliver either foam or bentonite slurry.

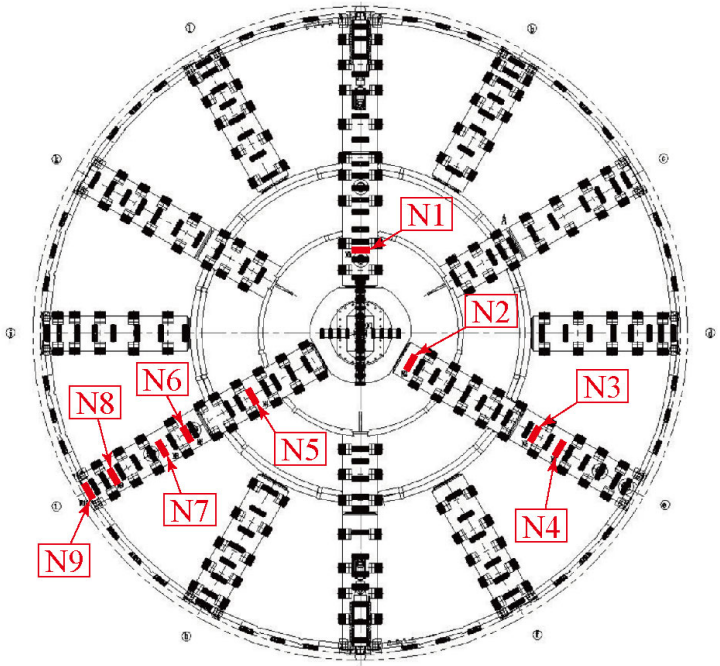


Figure 2. Layout of cutter tools and soil-conditioning agent injection ports on the cutterhead.

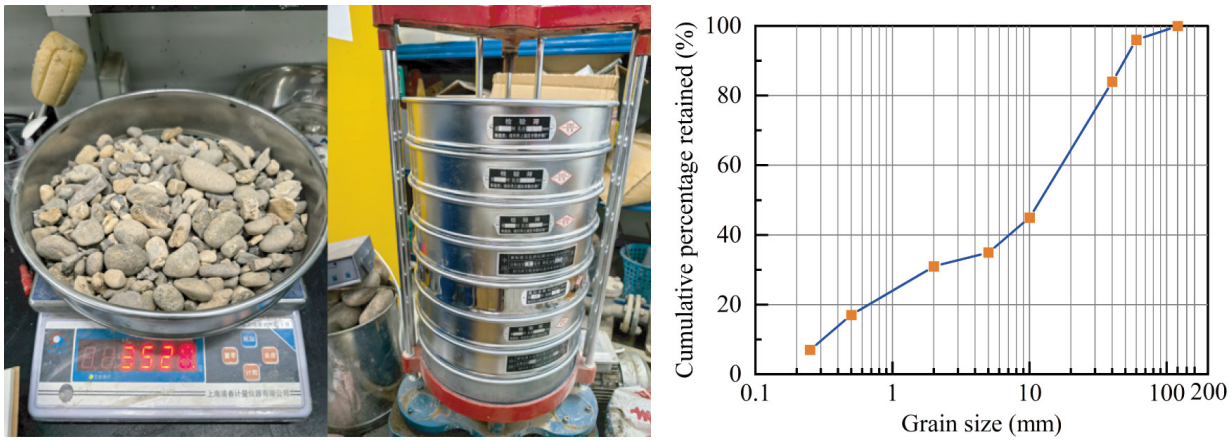
3. Laboratory Soil-Conditioning Tests

Laboratory testing was used to identify suitable foam-bentonite proportions for the MGZ-CQ-S2-V1 section. Sieve analysis first established the particle-size distribution of the excavated soil. Performance tests then determined suitable preparation parameters for the foaming agent and bentonite slurry. Finally, slump tests assessed the workability of the foam-bentonite-conditioned soil and screened the candidate proportions.

3.1. Test Materials

The undisturbed soil used in the tests was collected from the bottom of No. 2 southbound shield shaft in the MGZ-CQ-S2-V1 section. The sampling depth was close to the tunnel excavation depth and within the principal stratum traversed by the tunnel. The samples were sealed and transported to the laboratory for storage. The soil had an initial water content of approximately 3% and consisted mainly of sand, gravel and cobbles. We characterised its particle-size distribution by sieve analysis to support laboratory reconstruction and conditioning tests. A ZBSX-92A sieve shaker and seven round-hole sieves with apertures of 0.25–60 mm were used (Figure 3a). The shaker operated with a 25 mm swing stroke, a shaking frequency of 221 cycles · min^{-1} and a tapping frequency of 147 cycles · min^{-1}. Each specimen was sieved for 5 min. Four replicate specimens were tested, and their mean was reported. Particles measuring 10-40 mm accounted for approximately 39% of the field soil (Figure 3b). The coefficients of uniformity C_U and curvature C_C were 78.57 and 1.88, respectively, indicating a well-graded sandy cobble soil.

DY-978 foam concentrate, a product commonly used in engineering practice, served as the conditioning material. A Z-04 benchtop foam generator was used to produce the foam. Sodium bentonite was used to prepare the slurry.



(**a**) (**b**)

Figure 3. Particle-size analysis and particle-size distribution of the original excavated soil: (**a**) Apparatus for the particle-size analysis of the original excavated soil; (**b**) Particle-size distribution curve of the original excavated soil.

3.2. Foaming-Agent Performance

Foam expansion ratio and half-life were used to compare foaming capacity and stability across foaming-agent concentrations. The expansion ratio was defined as the generated foam volume divided by the initial solution volume. Half-life was the time required for the drained liquid to reach 50% of the initial solution mass. For each mixture, 600 g of solution was prepared according to Table 1. After foaming, the foam volume was measured in a graduated cylinder, and the foam was transferred to a 1400 mL funnel for the half-life measurement [2]. Each concentration was tested in triplicate, and the mean was reported.

Table 1. Preparation schemes for foam solutions with different mass concentrations.

Foam Concentration (%)	Foam Concentrate (g)	Water Mass (g)	Temperature (°C)
2	12	588	25
3	18	582	
4	24	576	
5	30	570	
6	36	564	
7	42	558	

Foam expansion ratio and half-life both varied non-monotonically with foaming-agent concentration (Figure 4a,b). The expansion ratio peaked at 28 at a concentration of 6%, whereas the half-life peaked at 1136 ± 20 s at 5% and declined at higher concentrations. The two metrics therefore responded differently to concentration. EPB conditioning requires sufficient foam to fill voids in coarse-grained soil and sufficient stability to resist dissipation during mixing and transport [18]. The test results showed that the foaming agent at a mass concentration of 5% combined high foaming capacity with good stability, balancing void-filling performance and effect duration. Therefore, 5% was selected as the preferred concentration among those tested.

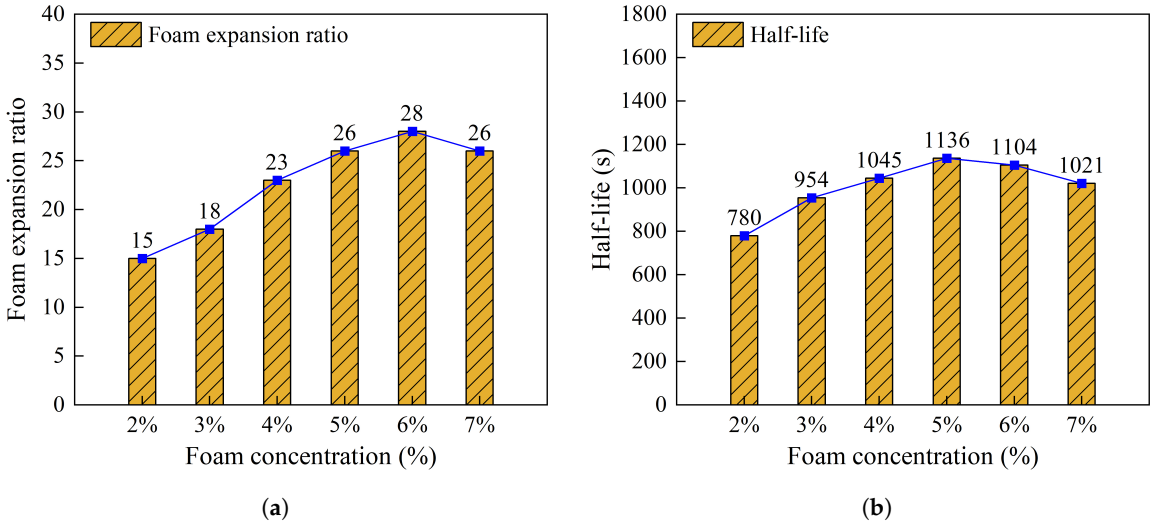


Figure 4. Effects of foaming-agent concentration on foam expansion ratio and half-life: (**a**) Variation in foam expansion ratio with foaming-agent concentration; (**b**) Variation in foam half-life with foaming-agent concentration.

3.3. Bentonite-Slurry Performance

Marsh funnel tests were used to identify a bentonite-slurry concentration and hydration time suitable for soil conditioning. Sodium-bentonite slurries with mass concentrations of 6–10% were prepared, and their flow times were measured at different hydration times. Each concentration-time combination was tested in triplicate, and the mean was reported [6].

Marsh funnel flow time was measured over 0–24 h for each slurry concentration (Figure 5). Bentonite slurry must remain sufficiently viscous for conditioning while retaining the flowability required for transport and pumping. Engineering practice generally adopts a Marsh funnel flow time of 40–60 s as a suitable range [19]. The 6% and 7% slurries remained relatively fluid throughout hydration, whereas the 9% and 10% slurries exceeded 60 s at later stages and did not meet the pumping requirement. After 24 h, the 8% slurry had a flow time of 50.25 ± 0.75 s, and its viscosity changed only gradually after 12 h. Therefore, considering both slurry viscosity and pumpability, the bentonite slurry with a mass concentration of 8% and a swelling time of 24 h was selected as the optimal formulation within the tested range and used in subsequent soil-conditioning tests.

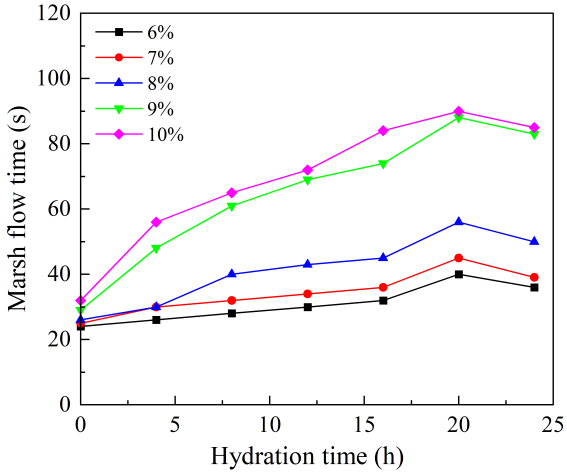


Figure 5. Marsh funnel flow time of bentonite slurries with different mass concentrations.

3.4. Slump Tests

Laboratory slump tests quantified the flowability, plasticity and workability of the conditioned soil and were used to identify foam and bentonite dosages suitable for field application [20]. We first determined the bentonite-slurry injection ratio and then tested combined foam-bentonite conditioning at different foam dosages.

Conditioning-agent dosage was normalised to the original soil volume. The bentonite injection ratio (BIR) and foam injection ratio (FIR) were defined as the injected bentonite-slurry volume and generated foam volume, respectively, divided by the original soil volume. They were calculated using Equations (1) and (2):

$$BIR = \frac{V_b}{V_s} \times 100\% \quad (1)$$

$$FIR = \frac{V_f}{V_s} \times 100\% \quad (2)$$

where V_b, V_f and V_s denote the volumes of injected bentonite slurry, generated foam and original soil, respectively.

3.4.1. Bentonite Conditioning

The tests followed the Standard for Test Method of Performance on Ordinary Fresh Concrete (GB/T 50080-2016) [21] and used a standard slump cone. The cone was 30 cm high, with top and bottom diameters of 10 and 20 cm, respectively. The standard applies to concrete with a maximum nominal aggregate size of 40 mm. Because cobbles larger than 40 mm accounted for approximately 17% of the total mass of the original soil sample and exceeded the allowable particle-size limit, they were replaced before testing with an equal mass of 5–40 mm cobbles with a comparable gradation [22–24]. Because this treatment alters the particle-size distribution, pore structure, and specific surface area of the undisturbed soil, the slump test was used only to preliminarily screen the candidate mixtures. The final scheme was selected based on full-scale DEM evaluation. Each batch of soil and conditioning agent was mixed to uniformity, placed in the cone in layers and allowed to stand for 60 s. The cone was then raised vertically at a uniform rate over approximately 5 s. Once deformation had ceased, slump was measured as the difference between the original cone height and the highest point of the soil [25]. The angle of repose, uniformity, flowability, plasticity and water separation were also recorded. Each mixture was tested in triplicate, and the mean was reported.

As BIR increased from 6% to 14%, the slump increased overall from 150 $\pm$ 5.2 to 185 $\pm$ 7.1 mm, whereas the angle of repose decreased from approximately 43° $\pm$ 1.6° to 25° $\pm$ 0.9° (Figure 6). These trends indicate that increasing the bentonite-slurry dosage enhanced the flowability of the conditioned soil. At BIR = 12%, the soil had a slump of 168 $\pm$ 6.4 mm and an angle of repose of 30° $\pm$ 1.1°, with favourable flowability and plasticity and no obvious water separation. Considering both flowability and workability, BIR = 12% was therefore selected as the fixed bentonite injection ratio for the subsequent combined foam-bentonite conditioning tests.

3.4.2. Combined Foam-Bentonite Conditioning

The combined-conditioning tests used the BIR selected above. The bentonite-slurry concentration was fixed at 8%, BIR at 12% and foaming-agent concentration at 5%, while FIR was varied from 10% to 50%. Slump, angle of repose, flowability, plasticity and water separation were used to assess performance at each foam dosage. The resulting soil morphologies are shown in Figure 7.

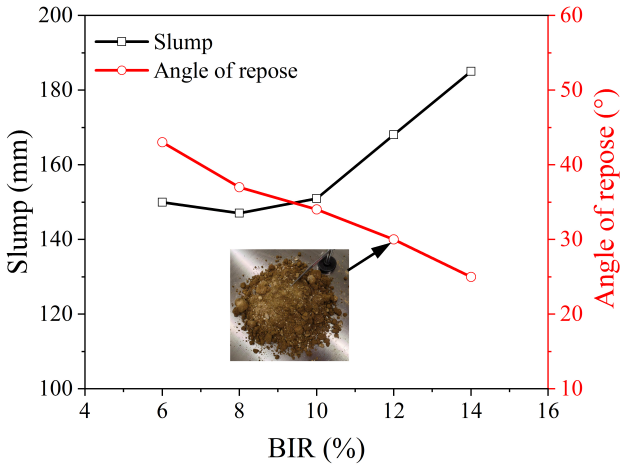


Figure 6. Effects of BIR on the slump and angle of repose of bentonite-conditioned soil.

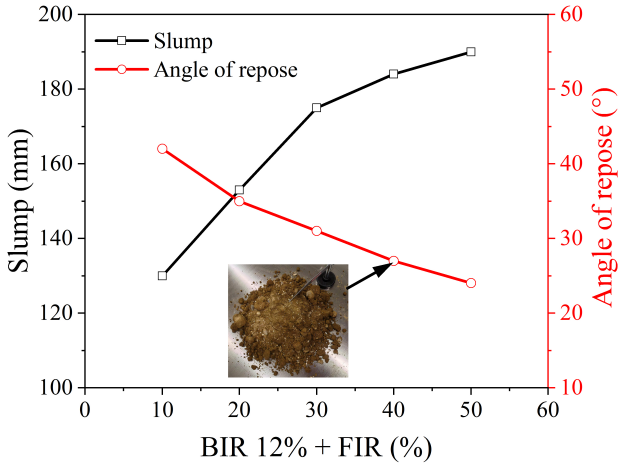


Figure 7. Effects of FIR on the slump and angle of repose of foam-bentonite-conditioned soil (BIR = 12%).

As FIR increased from 10% to 50%, the slump of the conditioned soil increased from 130 ± 5.5 to 190 ± 7.2 mm, whereas the angle of repose decreased from 42° ± 1.5° to 24° ± 0.8° (Figure 7), indicating that increasing the foam dosage enhanced soil flowability. The standard deviations of the slump and angle of repose across the groups ranged from 5.5 to 7.2 mm and from 0.8° to 1.5°, respectively. The overall variability was low, indicating good experimental repeatability. The most pronounced improvement occurred as FIR increased from 10% to 30%, with a 45-mm increase in slump and an 11° decrease in the angle of repose. Beyond an FIR of 30%, both the increase in slump and the decrease in the angle of repose became progressively smaller. At FIRs of 30% and 40%, the slump values were 175 ± 5.9 and 184 ± 6.3 mm, respectively, while the corresponding angles of repose were 31° ± 1.1° and 27° ± 0.9°. The corresponding ranges showed partial overlap. When FIR reached 50%, the slump increased only to 190 ± 7.2 mm and the angle of repose decreased to 24° ± 0.8°. These results indicate that, although the conditioned soil exhibited greater flowability at an FIR of 40%, the overall difference between the two schemes was limited, and both satisfied the flow-plasticity and workability requirements for spoil conditioning in this tunnel section. Considering both the improvement in flowability and foam consumption, the combined foam-bentonite conditioning schemes with FIRs of 30% and 40% were considered suitable for the studied tunnel section, with the bentonite slurry and foaming-agent solution prepared at mass concentrations of 8% and 5%, respectively, and BIR fixed at 12%.

4. Numerical Simulation Method

4.1. Shield Excavation Model

A shield excavation model was developed to test whether the two laboratory-selected schemes remained suitable at construction scale. The model reproduced the shield geometry, cutterhead layout, ground conditions and operating parameters of the project. Geometry, equipment settings and motion boundaries were identical for both schemes; only the calibrated ground-particle parameters differed. The initial self-weight stress state was established through gravitational deposition of the particles. Groundwater and seepage effects were neglected because the groundwater table was below the tunnel invert. The model focused on the short-term excavation response near the cutterhead. Overexcavation, the shield-tail gap and synchronous grouting, which mainly affect deformation after shield-tail passage, were excluded.

Discrete element simulations were performed in Altair EDEM 2024 [26]. The model comprised the sandy cobble ground, cutterhead, soil chamber and screw conveyor [27] (Figure 8). The model was established at a 1:1 geometric scale relative to the engineering prototype. The ground domain was 12 m wide, 25 m high and 2 m long in the tunnelling direction. The actual tunnel cover of 14.5 m was adopted, and the cutterhead was located 1.4 m from each lateral boundary. This configuration preserved the actual geometric relationships among the cutterhead dimensions, tunnel depth and overlying ground, providing representative engineering-scale conditions for evaluating the transmission of excavation-induced disturbance to the ground surface and the resulting settlement response. Computational coarse-graining reduced the particle count while preserving the particle-size composition and contact-force transmission characteristics [28]. As shown in Table 2, the ground was discretised using equivalent spherical particles. The model width and cutterhead diameter were taken as characteristic dimensions, giving ratios of 30 and 22.8 to the maximum equivalent particle diameter, respectively. Both satisfied the recommended minimum ratio of 20 [29]. Four equivalent particle-size groups were defined according to the particle-size distribution in Section 1. The ground model contained a total of 2.55×10^5 particles. The Rayleigh critical time step was 9.7987×10^{-4} s, and the solver used 15% of this value. Before excavation, the particle bed settled under a gravitational acceleration of 9.81 m $\cdot$ s^{-2} until a stable initial stress state developed. The excavation chamber was prefilled with soil particles to establish a full-chamber condition, thereby minimising interference from transient particle collisions during initial filling when extracting the cutter-force data. Static equilibrium was assumed when the total kinetic energy reported by EDEM reached 0 J within numerical precision and remained stable; this deposited state provided the initial condition for excavation [30].

Table 2. Prototype and equivalent particle-size distributions used in the DEM model.

Actual Particle-Size Range (mm)	Equivalent Particle-Size Range (mm)	Particle Fraction (%)
>40	200–400	17
5–40	100–200	46
0.25–5	50–100	29
<0.25	<50	8

A full-scale geometric model of the cutterhead, soil chamber and screw conveyor reproduced cutter loading and the transport and discharge of conditioned soil [31,32]. The cutterhead rotated at 1.2 rpm, the shield advanced at 40 mm $\cdot$ min^{-1} and the screw conveyor rotated at 15 rpm. Table 3 lists the motion settings and material properties of the shield components.

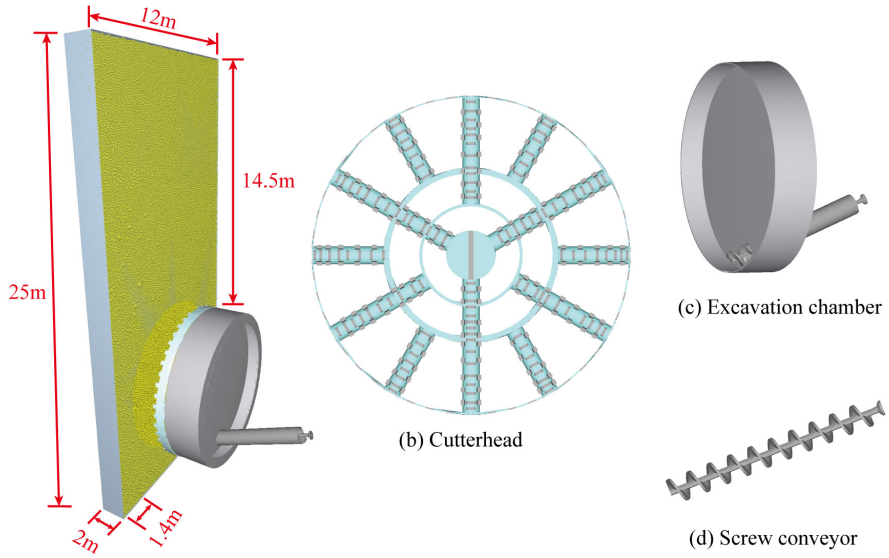


Figure 8. Full-scale EDEM shield tunnelling model and its main components.

Table 3. Operating and material parameters of the shield machine model.

Parameter	Value	Unit
Cutterhead rotational speed	1.2	rpm
Advance speed	40	mm/min
Screw conveyor rotational speed	15	rpm
Shear modulus of shield model	80,000	MPa
Density of shield model	7800	kg/m^3
Poisson's ratio of shield model	0.25	–

4.2. Contact-Model Selection and Calibration

In soil–tunnel interaction analyses, continuum methods commonly employ pressure-dependent yield models, such as the Drucker–Prager model, to describe the nonlinear elastoplastic behaviour of sandy soils [33]. Building on this framework, some studies have further considered shear deformation and nonlocal failure [34]. Previous finite-element studies have shown that the choice of constitutive relation and boundary conditions may affect the calculated soil–structure interaction response [35]. Unlike continuum models, in which macroscopic yield criteria are predefined, DEM generates the macroscopic response through particle contact, sliding, rolling and the evolution of contact networks. Therefore, the reliability of DEM simulations depends primarily on the choice of contact model and the macroscopic calibration of its parameters.

Bentonite and foam promote adhesion and agglomeration among excavated-soil particles, giving the conditioned material measurable interparticle cohesion. Particle-particle contacts were therefore represented using the Hertz–Mindlin with JKR model [36], with the standard rolling-friction model accounting for rolling resistance. The contact law combines Hertzian nonlinear elasticity, collision damping and Mindlin tangential contact with a JKR adhesive force governed by surface energy. Tangential friction is also included. Adhesion between particles and equipment walls was neglected; these contacts were represented using the Hertz–Mindlin no-slip model with elastic contact, collision damping and tangential friction [37,38].

Discrete element calibration adjusts microscopic contact parameters until the model reproduces the macroscopic mechanical and flow behaviour measured in the laboratory. Because the relationship between microscopic parameters and macroscopic responses is

non-unique [39], calibration used both triaxial compression and slump tests. These tests constrained the shear response and flow behaviour of the conditioned soil, respectively.

Numerical triaxial calibration used a cylindrical EDEM specimen 50 mm in diameter and 100 mm high. To accommodate the triaxial specimen and slump cone, the characteristic size of each particle fraction was scaled by 1:80 while preserving the relative particle-size distribution [29]. The JKR surface energy was set to 0 during triaxial calibration to represent the negligible cohesion of the unconditioned sandy cobble soil. The particle shear modulus and the interparticle coefficients of static and rolling friction were subsequently calibrated by iteratively adjusting their values until the numerical results agreed with the geotechnical investigation results. Strain-controlled loading under confining pressures of 100, 200 and 300 kPa produced the axial stress–strain curves and peak strengths (Figure 9a). Macroscopic shear-strength parameters were then back-calculated using the Mohr–Coulomb criterion. Based on the numerical triaxial compression tests, the interparticle rolling friction, static friction and restitution coefficients were determined to be 0.5, 0.25 and 0.75, respectively. The numerical tests yielded a cohesion of 0 and an internal friction angle of 33.89° (Figure 9b), which were close to the corresponding values of 0 and 35°, respectively, reported for cobble and rounded-gravel layer ⑦ in the geotechnical investigation. The 3.18% relative error in internal friction angle indicates that the calibrated parameters reproduce the macroscopic shear strength of cohesionless soil [40,41].

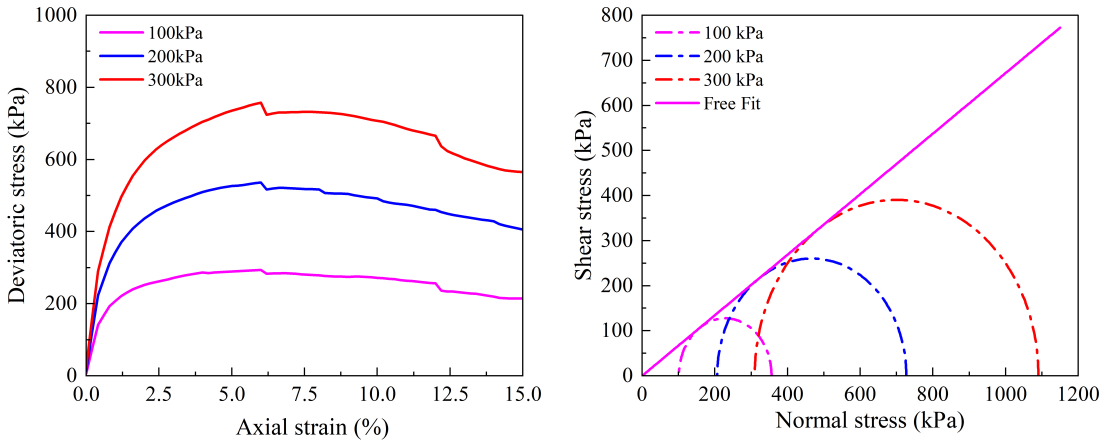


Figure 9. Stress-strain responses and strength envelope obtained from triaxial calibration: (**a**) Deviatoric stress–axial strain curves under different confining pressures; (**b**) Mohr–Coulomb strength envelope.

The numerical slump test reproduced the laboratory geometry. The cone was 30 cm high, with top and bottom diameters of 10 and 20 cm, respectively. After the particles reached equilibrium, the cone was raised vertically at 30 mm · s^{-1}. Once the particles had stabilised, the specimen height was measured and the slump and angle of repose were calculated (Figure 10).

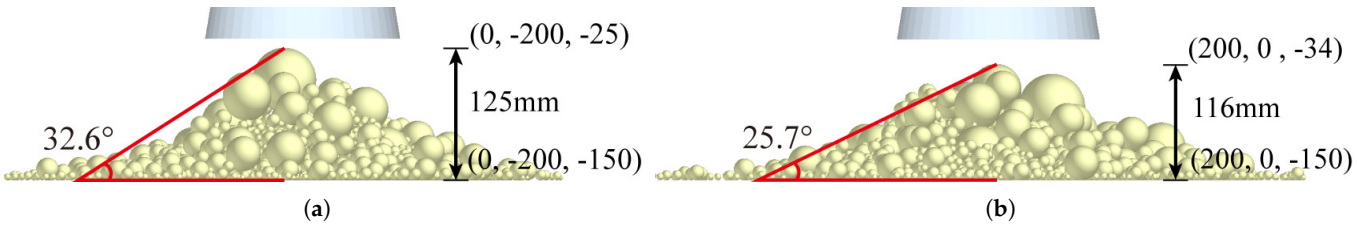


Figure 10. DEM slump calibration results for the two candidate soil-conditioning schemes: (**a**) Numerical slump profile of Scheme A; (**b**) Numerical slump profile of Scheme B.

The measured slump and angle of repose for the two conditioning schemes served as calibration targets. Particle-contact parameters and surface energy were adjusted iteratively until the simulated deposit geometry and characteristic values matched the laboratory results [42]. The same coefficient of restitution was used for both schemes to prevent differences in damping from affecting the comparison. Table 4 lists the calibrated parameters.

Table 4. Calibrated DEM contact parameters for the two candidate soil-conditioning schemes.

Contact Parameter	Particle–Particle Contact		Particle–Geometry Contact
	Slump 175 mm	Slump 184 mm	
Density (kg/m^3)	2000	2000	–
Poisson's ratio	0.3	0.3	–
Shear modulus (MPa)	60	60	–
Coefficient of restitution	0.75	0.75	0.25
Coefficient of static friction	0.14	0.10	0.40
Coefficient of rolling friction	0.80	0.50	0.001
JKR surface energy (J/m^2)	1.2	1.0	–

The calibration model and full-scale excavation model used the same Hertz–Mindlin with JKR contact law. The calibrated shear modulus, coefficient of restitution, coefficients of static and rolling friction and JKR surface energy were assigned directly to the full-scale model as equivalent contact parameters, without additional scaling factors. The quantities transferred between the two models were the contact constitutive parameters rather than the contact stiffnesses or forces generated in the calibration model. At the full scale, EDEM recalculated the contact stiffness, damping force and JKR adhesive force according to the equivalent particle radii, contact overlap and relative motion, thereby adapting the contact response to the current particle scale.

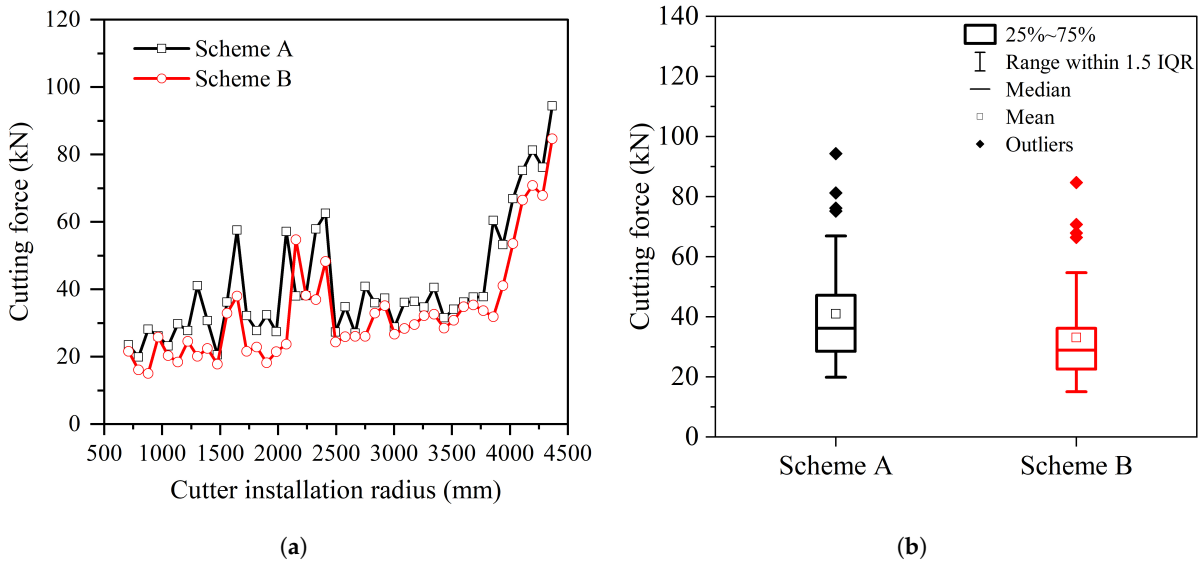
5. Numerical Comparison of Soil-Conditioning Schemes

The slump tests in Section 3.4 identified two candidate schemes. Scheme A used an 8% bentonite slurry at BIR = 12% and a 5% foaming-agent solution at FIR = 30%; Scheme B used the same materials and BIR but FIR = 40%. Full-scale simulations compared their cutter forces, cutterhead loads and ground-settlement responses to assess their suitability for tunnelling in sandy cobble strata.

5.1. Effects on Cutter and Cutterhead Loads

To characterise the overall force levels of ripper cutters at different installation radii, the arithmetic mean of all cutting-force samples recorded from the start of cutterhead advancement to the end of the simulation was calculated for each cutter (Figure 11a). These cutter-specific mean values were then used as samples to characterise their distribution (Figure 11b). Ripper-cutter force increased with installation radius under both schemes and fluctuated locally (Figure 11a). At radii of 965–3855 mm, most forces ranged from 20.5 to 41.1 kN. Beyond 3940 mm, force rose rapidly and peaked at 94.4 kN under Scheme A and 84.7 kN under Scheme B. The mean cutting force decreased by 19.1%, from 40.955 kN in Scheme A to 33.128 kN in Scheme B. The standard deviation decreased by 10.26%, from 17.44 to 15.65 kN. The radial increase reflects the greater cutter linear velocity at larger radii, whereas local fluctuations may result from random particle contacts, collisions and force-chain reconstruction. The median, interquartile range, and upper bound were all

lower for Scheme B than for Scheme A, indicating that Scheme B reduced both the overall cutting-force level and its variability (Figure 11b).



(**a**) (**b**)

Figure 11. Radial and statistical distributions of ripper cutter force under the two soil-conditioning schemes: (**a**) Variation in ripper cutter force with installation radius; (**b**) Statistical distribution of ripper cutter force.

Under both schemes, total thrust rose rapidly at the start of excavation before reaching a dynamic steady state (Figure 12a). Cutterhead torque followed the same pattern (Figure 12b). The shield was considered to have entered the steady tunnelling stage when the total cutterhead thrust and torque ceased their initial rapid increase and fluctuated around relatively stable mean values without sustained upward or downward trends. Accordingly, the interval between time steps 2.4×10^5 and 12.2×10^5 was selected for the statistical analysis of the steady tunnelling stage. The maximum relative differences in total thrust and cutterhead torque were 47.85% and 18.25%, respectively, both occurring at time step 0.40823×10^5. At this point, excavation was still at an early stage, during which the cutterhead-ground contact area and particle load-bearing network were developing rapidly. The load build-up processes of the two schemes were not yet synchronised, resulting in large transient relative differences. After steady tunnelling was established, both thrust and torque fluctuated around relatively stable mean values, and the differences between the two schemes decreased accordingly.

During steady excavation, Scheme B produced lower thrust and torque than Scheme A. The mean total thrusts of Schemes A and B were 2758.75 and 2143.90 kN, respectively, representing a reduction of 22.29% in Scheme B. The corresponding standard deviation decreased by 3.84%, from 426.29 to 409.92 kN. The mean cutterhead torques were 13,645.75 and 12,542.14 kN·m, respectively, representing a reduction of 8.09% in Scheme B. The corresponding standard deviation decreased by 6.22%, from 2134.26 to 2001.44 kN·m. The maximum relative difference in ripper cutting force between the two schemes was 58.60% and occurred at an installation radius of 2070 mm (Figure 12c). Scheme B therefore had a greater effect on penetration resistance than on rotational resistance. The higher FIR likely improved soil flowability and lubrication, reducing interparticle friction and friction at the soil–cutterhead interface.

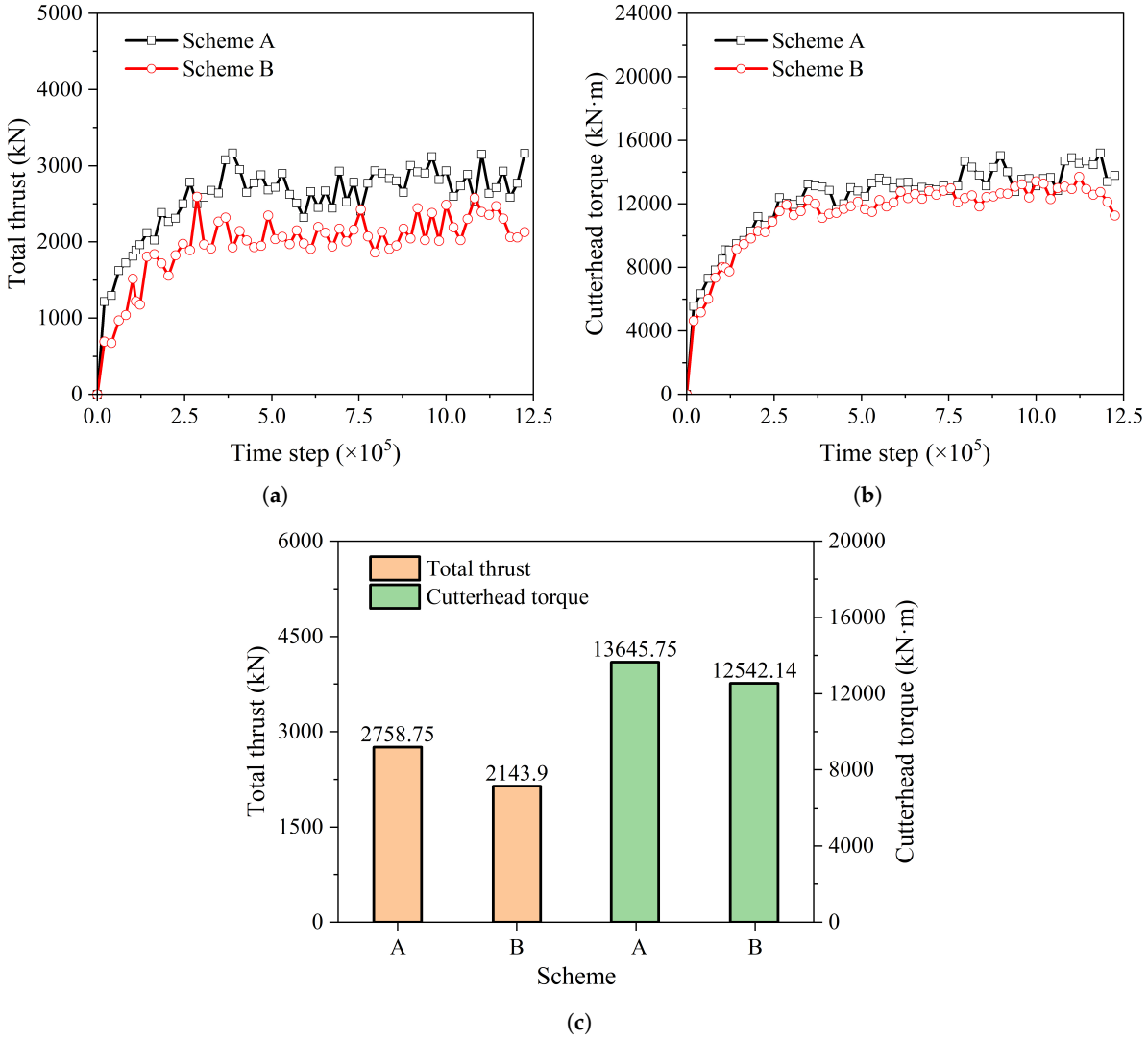


Figure 12. Time histories and stable-stage mean values of cutterhead loads under the two soil-conditioning schemes: (**a**) Time history of total cutterhead thrust; (**b**) Time history of cutterhead torque; (**c**) Comparison of the mean total thrust and cutterhead torque during the stable excavation stage.

5.2. Effects on Surface Settlement

Surface monitoring points were used to compare the magnitude and development of settlement under the two conditioning schemes. In a ground model measuring 12 m in transverse width and 2 m in the tunnelling direction, 20 surface-settlement monitoring points were evenly spaced along the y-axis and arranged symmetrically about the tunnel centreline (Figure 13). Ten points were positioned on each side of the tunnel centreline at a spacing of 0.6 m.

To suppress random particle-scale fluctuations, settlement at each location was calculated as the mean vertical displacement of surface particles surrounding the monitoring point. These averages defined the settlement profile and the maximum settlement. Under both schemes, settlement developed rapidly at the start of excavation and then slowed, reaching a stable value after approximately 6×10^5 time steps (Figure 14a). Final settlement was −17.7 mm under Scheme A and −13.4 mm under Scheme B, a reduction in magnitude of 4.3 mm, or approximately 24%. The maximum relative difference between the settlement time histories of the two schemes was 86.29%, occurring at time step 0.25×10^5. At this stage, surface settlement had only begun to develop, its absolute magnitude was small and

the particle contact network was still undergoing rapid adjustment. Consequently, a small absolute difference was substantially amplified when expressed as a relative difference. As excavation gradually stabilised, settlement in both schemes approached steady values, and the relative difference decreased markedly. Both schemes produced a trough centred near the tunnel centreline (Figure 14b). Maximum settlement decreased from −18.2 mm under Scheme A to −13.6 mm under Scheme B, a reduction in magnitude of 4.6 mm, or 25.3%, and the trough became shallower. In the central tunnel region, the relative difference in maximum settlement between the two schemes was 25.16%. The settlement troughs for both schemes exhibited some asymmetry, primarily owing to cutterhead rotation. The rotating cutterhead induced soil disturbances and displacements in different directions on either side of the excavation face. Considering the settlement time histories and spatial distributions together, under identical model assumptions, boundary conditions and tunnelling parameters, the scheme with a BIR of 12% and an FIR of 40% reduced the final and maximum settlement magnitudes by approximately 24.3% and 25.3%, respectively, compared with the scheme with a BIR of 12% and an FIR of 30%. This indicates more effective control of surface deformation induced by shield excavation.

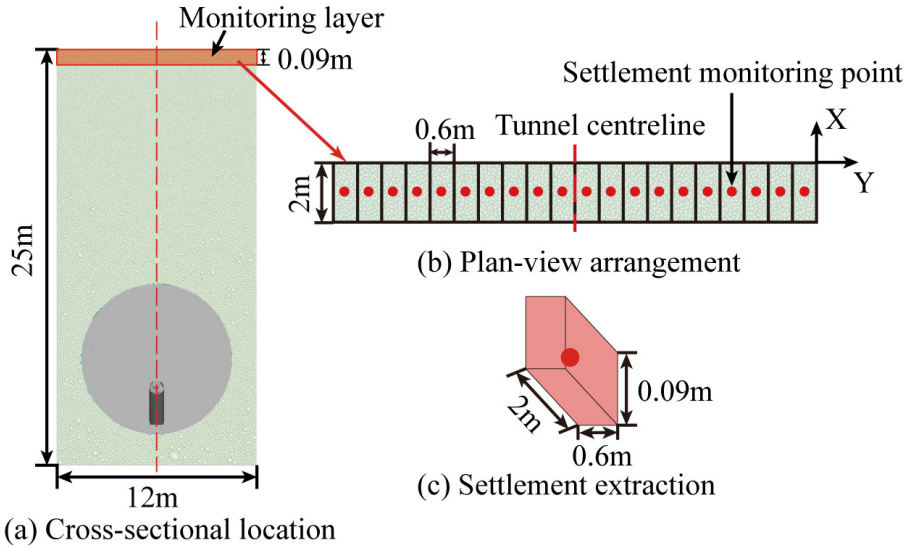


Figure 13. Layout of surface-settlement monitoring points in the DEM ground model.

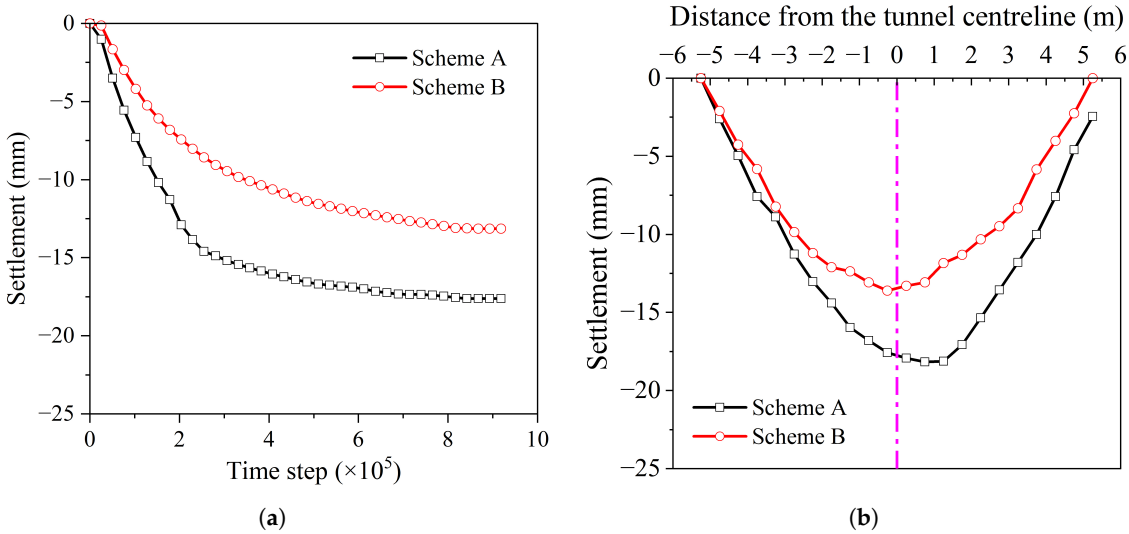


Figure 14. Surface-settlement time histories and transverse settlement troughs under the two soil-conditioning schemes: (**a**) Time history of surface settlement; (**b**) Transverse surface-settlement trough.

With the bentonite-slurry concentration fixed at 8%, BIR at 12% and foaming-agent concentration at 5%, increasing FIR from 30% to 40% reduced ripper cutter force, total thrust, cutterhead torque and surface settlement. Scheme B was therefore selected for field application.

6. Field Performance of the Selected Conditioning Scheme

To evaluate the effectiveness of the proposed method for selecting soil-conditioning schemes in sandy cobble strata, this section compares the numerical simulation results for Scheme B with its field performance.

6.1. Simulated Cutting Forces and Field Cutter Wear

The cutting forces acting on the cutters and the field-measured wear exhibited broadly consistent trends with installation radius (Figure 15). Below a radius of 1985 mm, cutting force was 15.3–41.2 kN and cumulative wear remained below 30 mm. Both measures increased between 1985 and 3515 mm, with local peaks at 2155–2580 mm. Beyond 3515 mm, force and wear rose markedly; the peripheral cutters reached a maximum force of 84.7 kN and maximum cumulative wear of 81 mm. The two datasets were fitted separately using exponential functions, and both fitted curves showed accelerating growth. The exponential coefficients were 0.3454 and 0.4293, with overlapping 95% confidence intervals, indicating similar radial variation patterns. Together with the Spearman correlation coefficient ($\rho = 0.790$, $p < 0.0001$), these results indicate a significant positive correlation between cutter cutting force and field-measured cumulative wear. Thus, outer cutters subjected to higher cutting forces generally exhibited greater cumulative wear. Although the principal high-value regions agreed, individual peaks did not coincide exactly. Wear accumulates over time and depends on cutter trajectory, cutting distance, particle hardness and collision frequency as well as load. Cutter force and cumulative wear therefore need not be linearly related.

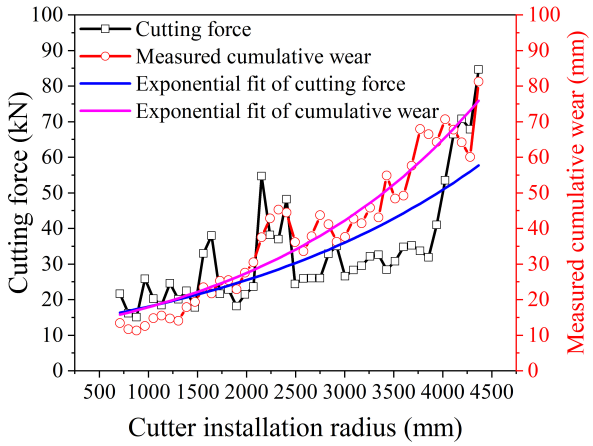


Figure 15. Radial variations in simulated cutter force and measured cumulative wear.

Because the cutterhead-ground axial contact force output by the DEM differs in physical composition and magnitude from the field-monitored total propulsion thrust, their absolute values should not be compared directly [43]. To compare their relative evolution during excavation, the simulated and measured values were normalised by their respective means [44]. For any load series (X), the normalised value is defined as:

$$X_i^* = \frac{X_i}{\overline{X}} \tag{3}$$

$$\bar{X} = \frac{1}{n}\sum_{i=1}^{n} X_i \quad (4)$$

where X_i is the i-th data point, $\bar{X}$ is the mean of the corresponding series over the selected comparison interval and n is the number of data points. After normalisation, a value of 1 represents the mean level; values greater than 1 indicate loads above the mean, whereas values less than 1 indicate loads below the mean.

The complete simulation time-step sequence represented the excavation of one ring and was aligned with the field monitoring period from the start to the completion of shield advancement for the corresponding ring (Figure 16a,b). Simulated total thrust and cutterhead torque rose rapidly at the start of excavation and then entered a fluctuating steady state. After alignment by excavation progress, the simulated and measured series showed similar normalised ranges, fluctuation patterns and overall trends during steady excavation. The normalised simulated and measured total thrusts ranged from 0.569–1.254 and 0.753–1.240, with standard deviations of 0.133 and 0.120, respectively. The two datasets exhibited similar levels of fluctuation throughout the full one-ring comparison interval. The normalised simulated torque was mainly distributed between 0.909 and 1.193, broadly comparable to the measured range of 0.749–1.199. The thrust discrepancy arose mainly because the DEM output primarily represented the axial cutterhead-ground contact force, whereas the field-measured total thrust also included shield-ground friction, seal resistance, and other mechanical resistances. The torque discrepancy may result from the model considering mainly particle-cutterhead contact resistance without fully accounting for resistance from the main bearing and sealing system. Overall, the normalised results indicate that the numerical model reasonably reproduced the overall evolution and relative fluctuations of cutterhead loads during steady tunnelling.

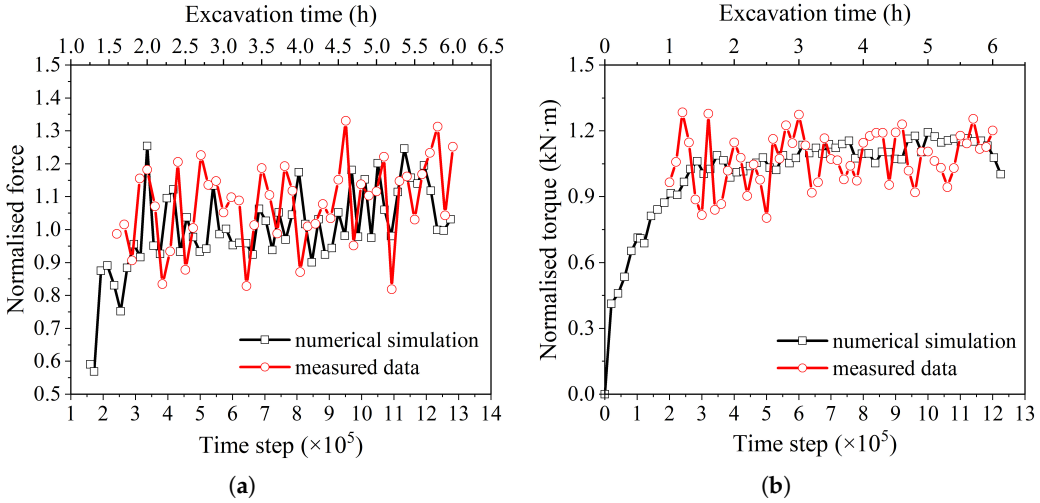


Figure 16. Normalised cutterhead-load responses for Rings 1-2: (**a**) Normalised axial-load response for Rings 1-2; (**b**) Normalised torque response for Rings 1-2.

6.2. Surface-Settlement Response

Settlement measured at monitoring point DB-30-02 was compared with the Scheme B simulation (Figure 17). Both curves developed rapidly during early excavation and then approached stable values. As excavation progressed, the simulation continued to accumulate settlement, whereas the measurement fluctuated between −11 and −12 mm before stabilising. Final simulated and measured settlements were −13.6 and −11.8 mm, respectively. The simulated magnitude exceeded the measurement by 1.8 mm, corresponding to a relative deviation of 15%, and was therefore slightly conservative. Later rebound and fluctuation in the measured curve may reflect ground heterogeneity, changes in operating

parameters, synchronous grouting and measurement error. By contrast, the model used idealised boundaries and uniform parameters, producing a smoother settlement history.

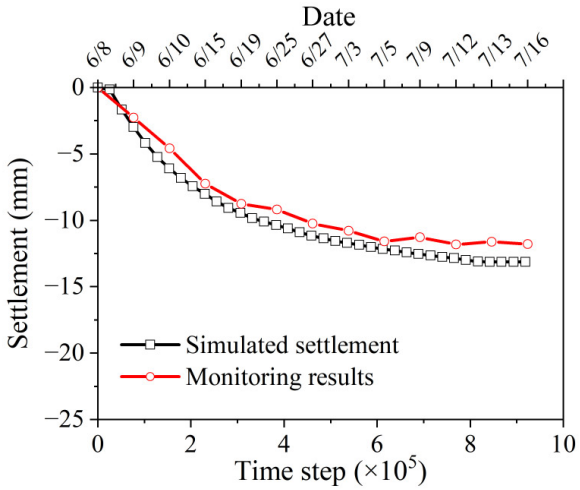


Figure 17. Comparison of EDEM-predicted and field-measured surface-settlement time histories at the monitoring point.

After calibration against triaxial compression and slump tests, the EDEM model reproduced the broad radial pattern of field cutter wear through its predicted cutter-force distribution. It also reproduced the relative evolution of total thrust and cutterhead torque, as well as the development of surface settlement, although settlement was slightly overpredicted. Agreement across these independent field responses supports the reliability of the full-scale discrete element model and the engineering feasibility of combining laboratory tests with simulation to select a soil-conditioning scheme.

7. Conclusions

This study combined laboratory screening, full-scale discrete element simulation and field validation to select a soil-conditioning scheme for EPB tunnelling in sandy cobble strata. Conditioning-agent performance and slump tests identified mixtures that met the flowability and workability requirements. Triaxial compression and slump tests calibrated the particle-contact parameters governing the mechanical and flow behaviour of conditioned soil. Cutter forces, cutterhead loads and surface settlement then provided construction-scale criteria for comparing the candidate schemes. The field response under the selected scheme was broadly consistent with the simulation. The principal conclusions are as follows:

1. Laboratory tests identified two suitable combined-conditioning schemes: an 8% bentonite slurry at BIR = 12% and a 5% foaming-agent solution at FIR = 30% or 40%. The corresponding slumps were 175 and 184 mm, and the angles of repose were 31° and 27°, respectively. Both mixtures showed favourable flowability and plasticity without obvious water separation.
2. The calibrated EDEM model enabled comparison of the excavation responses under the two soil-conditioning schemes and selection of the preferred scheme. With all other parameters fixed, increasing FIR from 30% to 40% reduced the mean ripper cutter force, mean steady-state total thrust and mean cutterhead torque by 19.10%, 22.29% and 8.09%, respectively. Final and maximum settlement decreased by 24.3% and 25.3%. Therefore, the conditioning scheme comprising an 8% bentonite slurry (BIR = 12%) and a 5% foaming-agent solution (FIR = 40%) reduced cutter and cutterhead loads while limiting excavation-induced ground deformation.

3. The calibrated EDEM model reproduced the broad radial correspondence between predicted cutter force and measured cutter wear. It also captured the trends of total thrust, cutterhead torque and surface settlement, although the settlement prediction was slightly conservative. The simulated settlement differed from the field-monitored settlement by 15%. Agreement across these field responses supports the use of the model to represent the principal loads and ground deformation during shield tunnelling in sandy cobble strata.
4. Combining laboratory screening with full-scale EDEM simulation provides a quantitative basis for selecting soil-conditioning schemes before construction. The approach links laboratory workability indices to cutter forces, total thrust and cutterhead torque, and surface settlement. Field monitoring supported the applicability of the selected scheme. This workflow can reduce field trial mixing and parameter adjustment while improving the efficiency of scheme selection.

This study considered only one project, one shield machine and a limited set of conditioning parameters; therefore, the conclusions remain dependent on the specific engineering conditions. Coarse-grained spherical particles cannot fully capture particle shape, interlocking, breakage or force-chain evolution. The model also simplified or omitted groundwater, chamber pressure, shield–ground friction, over-excavation, the shield-tail gap and synchronous grouting. The conditioned-soil parameters were not independently validated through mechanical testing. Field validation was limited to tunnelling data from Rings 1-2 and a single settlement-monitoring point, while cutter forces were validated only indirectly using cumulative wear. Comparisons of normalised thrust and torque reflect only the load-evolution trends and relative fluctuations and cannot assess the predictive accuracy of their absolute values.

Future work should validate the method across multiple projects under different geological, equipment and operating conditions. Parameter-sensitivity analysis, non-spherical or crushable particles, additional construction mechanisms and more extensive field-monitoring data should also be incorporated to further assess its applicability and reliability.

Author Contributions: Writing—original draft preparation, W.Z. and Z.L.; Writing—review and editing, W.Z., Z.L. and Z.Y.; Methodology, J.Z., T.W. and Z.Y.; Formal analysis, J.Z., T.W. and Z.Y.; Data investigation, J.Z., T.W. and Z.Y. All authors have read and agreed to the published version of the manuscript.

Funding: This research received no external funding.

Data Availability Statement: Some of the data, models and code that support the findings of this study are available from the corresponding author upon reasonable request.

Conflicts of Interest: The authors declare no conflicts of interest.

References

1. Yang, Z.; Shao, X.; Liu, Z.; Bai, Z.; Jiang, Y. Optimization and Field Validation of Soil Conditioning Scheme for EPB Shield Tunneling in Cobble–Boulder Stratum: Case Study on Beijing Metro Line 16. *Buildings* **2025**, *15*, 4429. [CrossRef]
2. Jiang, Y.; Tang, X.; Zhu, B.; Zhou, K.; Pan, Y.; Xu, C. Research on muck conditioning for EPB shield tunnelling in composite formation. *Sci. Rep.* **2024**, *14*, 30936. [CrossRef]
3. Wang, S.; Liu, P.; Gong, Z.; Yang, P. Auxiliary air pressure balance mode for EPB shield tunneling in water-rich gravelly sand strata: Feasibility and soil conditioning. *Case Stud. Constr. Mater.* **2022**, *16*, e00799. [CrossRef]
4. Sun, Y.; Liu, D.; Wang, G. Experimental Study on the Effects of New Foam on the Improvement of Sandy Soil for Earth Pressure Balance Shield. *Buildings* **2023**, *13*, 682. [CrossRef]
5. Sun, Y.; Zhao, D. Research and Experimental Application of New Slurry Proportioning for Slag Improvement of EPB Shield Crossing Sand and Gravel Layer. *Coatings* **2022**, *12*, 1961. [CrossRef]

6. Ling, F.; Wang, S.; Hu, Q.; Huang, S.; Feng, Z. Effect of bentonite slurry on the function of foam for changing the permeability characteristics of sand under high hydraulic gradients. *Can. Geotech. J.* **2022**, *59*, 1061–1070. [CrossRef]
7. Wang, L.; Zhu, W.; Qian, Y. Experimental study on the stratum applicability and mechanisms of bubble-slurry for earth pressure balance shields. *Front. Struct. Civ. Eng.* **2023**, *17*, 1387–1399. [CrossRef]
8. Wang, L.; Zhu, W.; Qian, Y.; Xing, H. The New Bubble-Slurry for Sand Conditioning during EPB Shield Tunnelling: A Laboratory Scale Study. *KSCE J. Civ. Eng.* **2023**, *27*, 2191–2201. [CrossRef]
9. Nong, X.; Bai, W.; Chen, J.; Zhang, L. Factorial Experiments of Soil Conditioning for Earth Pressure Balance Shield Tunnelling in Water-Rich Gravel Sand and Conditioning Effects' Prediction Based on Particle Swarm Optimization–Relevance Vector Machine Algorithm. *Buildings* **2024**, *14*, 2800. [CrossRef]
10. Lee, H.; Kim, D.Y.; Shin, D.; Oh, J.; Choi, H. Effect of foam conditioning on performance of EPB shield tunnelling through laboratory excavation test. *Transp. Geotech.* **2022**, *32*, 100692. [CrossRef]
11. Yang, Z.; Yang, X.; Ding, Y.; Jiang, Y.; Qi, W.; Sun, Z.; Shao, X. Characteristics of conditioned sand for EPB shield and its influence on cutterhead torque. *Acta Geotech.* **2022**, *17*, 5813–5828. [CrossRef]
12. Li, S.; Wan, Z.; Zhao, S.; Ma, P.; Wang, M.; Xiong, B. Soil conditioning tests on sandy soil for earth pressure balance shield tunneling and field applications. *Tunn. Undergr. Space Technol.* **2022**, *120*, 104271. [CrossRef]
13. Zhang, K.; Zhang, Z.; Liu, C. Laboratory and field tests on soil conditioning for earth pressure balance shield tunneling in composite strata with different sand-rock ratios. *Front. Struct. Civ. Eng.* **2025**, *19*, 411–426. [CrossRef]
14. Wang, L.; Hu, J.; Zhu, W.; Min, F. Effects of Conditioning Agents on the Undrained Shear Response and Pore-Scale Behavior of Sand for EPB Shield Tunneling. *Appl. Sci.* **2026**, *16*, 531. [CrossRef]
15. Wang, X.; Zhao, W.; Li, J.; Han, J.; Cheng, C.; Bai, Q.; Sun, D. Intelligent optimization of soil conditioning schemes based on earth pressure balance shield tunnelling data. *Tunn. Undergr. Space Technol.* **2026**, *173*, 107637. [CrossRef]
16. Qu, T.; Wang, S.; Hu, Q. Coupled Discrete Element-Finite Difference Method for Analysing Effects of Cohesionless Soil Conditioning on Tunneling Behaviour of EPB Shield. *KSCE J. Civ. Eng.* **2019**, *23*, 4538–4552. [CrossRef]
17. Lee, H.; Kim, H.K.; Hwang, B.; Yoon, Y.; Choi, H. Coupled DEM–FDM numerical model for EPB shield tunnelling simulation with foam conditioning. *Tunn. Undergr. Space Technol.* **2024**, *147*, 105718. [CrossRef]
18. Feng, Z.; Wang, S.; Qu, T.; Zheng, X.; Ling, F. Experimental study on workability and permeability of sandy soils conditioned with thickened foam. *J. Rock Mech. Geotech. Eng.* **2024**, *16*, 532–544. [CrossRef]
19. Davoodi, S.; Al-Rubaii, M.; Wood, D.A.; Al-Shargabi, M.; Mehrad, M.; Rukavishnikov, V.S. Hybrid Machine-Learning Model for Accurate Prediction of Filtration Volume in Water-Based Drilling Fluids. *Appl. Sci.* **2024**, *14*, 9035. [CrossRef]
20. Vinai, R.; Oggeri, C.; Peila, D. Soil conditioning of sand for EPB applications: A laboratory research. *Tunn. Undergr. Space Technol.* **2008**, *23*, 308–317. [CrossRef]
21. *GB/T 50080–2016* ; Standard for Test Method of Performance on Ordinary Fresh Concrete. Ministry of Housing and Urban-Rural Development of the People's Republic of China: Beijing, China, 2016.
22. Lin, S.Y.; Lin, P.S.; Luo, H.S.; Juang, C.H. Shear modulus and damping ratio characteristics of gravelly deposits. *Can. Geotech. J.* **2000**, *37*, 638–651. [CrossRef]
23. Zhao, M.; Kang, R.; Chen, S.; Wang, S.; Zhai, N.; Zhang, C. Study on the scale effect and mechanical properties of gravel materials in riverbed cover layers. *Sci. Rep.* **2024**, *14*, 30698. [CrossRef]
24. Liu, J.; Pan, J.; Wang, B.; Hu, C.; Liu, Q. Study on the shear and deformation characteristics of geogrid-reinforced gravelly soils based on large-scale triaxial tests. *Front. Earth Sci.* **2024**, *12*, 1287718. [CrossRef]
25. Martinelli, D.; Peila, D.; Campa, E. Feasibility study of tar sands conditioning for earth pressure balance tunnelling. *J. Rock Mech. Geotech. Eng.* **2015**, *7*, 684–690. [CrossRef]
26. Altair Engineering, Inc. *Altair EDEM*, version 2024.0; Computer Software; Altair Engineering, Inc.: Troy, MI, USA, 2024.
27. Zhu, C.; Huang, X.; Xu, C.; Yan, G.; Guo, J.; Liang, Q. Displacement Response Characteristics and Instability Risk Assessment of Excavation Face in Deep-Buried Shield Tunnel. *Buildings* **2025**, *15*, 2561. [CrossRef]
28. Coetzee, C. Particle upscaling: Calibration and validation of the discrete element method. *Powder Technol.* **2019**, *344*, 487–503. [CrossRef]
29. Cantor, D.; Ovalle, C. Sample size effects on the critical state shear strength of granular materials with varied gradation and the role of column-like local structures. *Géotechnique* **2025**, *75*, 29–40. [CrossRef]
30. Jeong, D.W.; Kim, M.S.; Choi, S.O.; Noh, S.Y.; Kim, Y.S.; Kim, W.S.; Baek, S.Y.; Kim, Y.J. Effect analysis of soil texture and water content on soil adhesive force based on the discrete element method. *Sci. Rep.* **2026**, *16*, 20708. [CrossRef]
31. Guo, H.; Zhang, G.; Mao, X.; Zan, J. A Novel Simplified Physical Model Testing Method for Ground Settlement Induced by Shield Tunnel Excavation. *Buildings* **2025**, *15*, 710. [CrossRef]
32. Wang, X.; Li, Y.; Wei, G.; Wei, X.; Yan, Z.; Yan, J.; Li, B. Model Design and Application for Excavation Face Stability in Upward Shield Tunneling. *Buildings* **2024**, *14*, 2514. [CrossRef]
33. Drucker, D.C.; Prager, W. Soil mechanics and plastic analysis or limit design. *Q. Appl. Math.* **1952**, *10*, 157–165. [CrossRef]

34. Zhang, T.; Zhou, X.P.; Qian, Q.H. Drucker-Prager plasticity model in the framework of OSB-PD theory with shear deformation. *Eng. Comput.* **2023**, *39*, 1395–1414. [CrossRef]
35. Savvides, A.A.; Tsotoulidi, V. Influence of nonlinear Lysmer dashpots on seismic soil-structure interaction: A comparative finite element study. *J. Eng. Appl. Sci.* **2026**, *73*, 375. [CrossRef]
36. Yang, Y.; Li, X.G.; Li, H.Y.; Guo, Y.D.; Fang, Y.R. Assessing clogging potential and optimizing driving parameter of slurry shield tunneling in clay stratum assisted with CFD–DEM modeling. *Undergr. Space* **2024**, *14*, 197–218. [CrossRef]
37. Di Renzo, A.; Di Maio, F.P. Comparison of Contact-Force Models for the Simulation of Collisions in DEM-Based Granular Flow Codes. *Chem. Eng. Sci.* **2004**, *59*, 525–541. [CrossRef]
38. Jin, H.; Wang, E.; Liu, X.; Xu, Z.; Wang, M.; Yuan, D. Micro-Mechanism of Shield–Soil Interaction during Shield Tunneling Based on DEM–MBD Coupling Simulation. *Comput. Geotech.* **2025**, *186*, 107439. [CrossRef]
39. Coetzee, C. Review: Calibration of the discrete element method. *Powder Technol.* **2017**, *310*, 104–142. [CrossRef]
40. Rackl, M.; Hanley, K.J. A methodical calibration procedure for discrete element models. *Powder Technol.* **2017**, *307*, 73–83. [CrossRef]
41. Li, P.; Cui, X.; Wei, Y.; Xia, J.; Wang, X. Calibration Method of Mesoscopic Parameter in Sandy Cobble Soil Triaxial Test Based on PFC3D. *Front. Struct. Civ. Eng.* **2023**, *17*, 1924–1933. [CrossRef]
42. Cheng, P.; Zhuang, X.; Zhu, H.; Li, Y. The Construction of Equivalent Particle Element Models for Conditioned Sandy Pebble. *Appl. Sci.* **2019**, *9*, 1137. [CrossRef]
43. Bilgin, N.; Yüksel, A. The Effect of EPB Face Pressure on TBM Performance Parameters in Different Geological Formations of Istanbul. *Tunn. Undergr. Space Technol.* **2023**, *138*, 105184. [CrossRef]
44. Bilgin, N.; Acun, S. The Effect of Rock Weathering and Transition Zones on the Performance of an EPB–TBM in Complex Geology near Istanbul, Turkey. *Bull. Eng. Geol. Environ.* **2021**, *80*, 3041–3052. [CrossRef]

Disclaimer/Publisher's Note: The statements, opinions and data contained in all publications are solely those of the individual author(s) and contributor(s) and not of MDPI and/or the editor(s). MDPI and/or the editor(s) disclaim responsibility for any injury to people or property resulting from any ideas, methods, instructions or products referred to in the content.